Supporting Information

Seed Crystal Phase Governs Interfacial Coherence and Strain in Janus $Cu_{2-x}S$/CdS Heteronanorods

Sen Yang, Yuhang Wang, Fenghuan Zhao, Xiaobin Xie, Yue Liu, Hongyu Zhao, Ziwei Liu, Chunchao Hou, Junjie Qin, Bohua Dong, Lixin Cao and Chenghui Xia **

S. Yang, Y. Wang, H. Zhao, Z. Liu, C. Hou, J. Qin, B. Dong, L. Cao, C. Xia
School of Materials Science and Engineering, Ocean University of China, Qingdao 266404, China
E-mail: caolixin@ouc.edu.cn; c.xia@ouc.edu.cn

F. Zhao
Department of Mechanical and Electrical Engineering, Rizhao Polytechnic, 16 Yantai North Road, Rizhao City, Shandong Province, 276826, PR China

X. Xie
Guangdong Provincial Key Laboratory of Optical Information Materials and Technology & Institute of Electronic Paper Displays, South China Academy of Advanced Optoelectronics, South China Normal University, Guangzhou 510006, China

Y. Liu
National Engineering Laboratory of Eco-Friendly Polymeric Materials, Key Laboratory of Green Chemistry and Technology of Ministry of Education, College of Chemistry, Sichuan University, Chengdu 610064, China

Characterization

Absorption spectra were obtained by dispersing the products in 3 mL of cyclohexane and transferring the suspension into sealed quartz cuvettes inside a glovebox. The spectra were recorded on a Shimadzu UV-2550 UV-Vis spectrophotometer. Powder X-ray diffraction (XRD) patterns were collected on a Bruker D8 Advance diffractometer with Cu Kα radiation (λ=1.5406 Å). Morphology and particle size were characterized by transmission electron microscopy (TEM, JEM-2100EX) using copper grids. High-resolution TEM (HRTEM) and scanning TEM–high-angle annular dark-field (STEM-HAADF) images were obtained using a Thermo Fisher Scientific Spectra 300 S/TEM operated at 300 kV with a camera length of 115 mm. STEM=EDS elemental mapping was performed using the ChemiSTEM detector. Fourier-transform infrared (FT-IR) spectra were measured on a Nicolet IS50 spectrometer in the range of 400=4000 cm^{-1}. X-ray photoelectron spectroscopy (XPS) measurements were carried out on a Thermo Scientific ESCALAB 250 Xi spectrometer equipped with a twin crystal monochromator and a 180° hemispherical analyzer, using Al Kα radiation (1486.6 eV, 72 W, 400 μm spot size). The pass energies were set at 200 eV for survey scans and 50 eV for high-resolution scans. The binding energies were calibrated to the C 1s peak of surface-adsorbed carbon at 284.80 eV. Inductively coupled plasma mass spectrometry (ICP-MS) measurements were performed on an Agilent Technologies 5110 ICP-MS system equipped with a dichroic spectral combiner and a VistaChip II CCD detector. Dried samples were digested in HNO_3 (69.5%) and diluted with 5% HNO_3 to achieve analyte concentrations within the ppb range.

Photoelectrochemical measurements

Photoelectrochemical measurements were carried out on a CHI660E electrochemical workstation (Shanghai Chenhua) using a 500 W Xe lamp (Beijing Zhonjiao Jinyuan) as the light source (100 $mW \cdot cm^{-2}$). A standard three-electrode system was employed, with the working electrode prepared by spin-coating the catalyst dispersion onto a 1 × 1 cm^2 FTO glass substrate followed by vacuum drying at 60 °C overnight. A 0.5 M Na_2SO_4 aqueous solution was used as the electrolyte. Transient photocurrent-time curves were recorded under a bias of -0.4 V vs. Ag/AgCl with light on-off cycles. Electrochemical impedance spectroscopy was measured in a frequency range of 0.1 Hz to 10 kHz. Mott-Schottky measurements were carried out in a potential range from -1 V to +1 V at a frequency of 1000 Hz. Electrochemical double layer capacitance (CDL) was derived from Cyclic voltammetry (CV) curves at non-faradaic region. CV experiments were conducted at various scan rates (20, 40, 60, 80 and 100 mV s^{-1}) within a non-faradaic potential window from -0.9 V to -0.8 V vs. RHE.

Photocatalytic hydrogen evolution performance test

Photocatalytic hydrogen evolution was performed on an online photocatalytic hydrogen production system (CEL-SPH2H, Beijing Zhongjiao Jinyuan). Typically, 5 mg of catalyst was dispersed in 10 mL of a mixed aqueous solution of Na_2S/Na_2SO_3 (0.23 M/0.35 M). Prior to illumination, the reactor was purged with high-purity nitrogen (99.99%) for 30 min to remove air. A 500 W Xe lamp (Beijing Zhonjiao Jinyuan) with a cutoff filter (λ ≥ 420 nm) was used as the light source, with an intensity of 100 $mW \cdot cm^{-2}$. A circulating water system maintained the reaction temperature at 5 ± 0.2 °C. The evolved hydrogen was quantitatively analyzed by gas chromatography (GC7920-TF22A2, Beijing Zhongjiao Jinyuan) and monitored over 4 h. The apparent quantum yields (AQY) were measured on PLD-QY1000 (Perfect, China). The reaction solution was identical to that used in the above HER experiments. Monochromatic light at 420 nm and 550 nm was employed for the AQY measurement. AQY was calculated by the following equation:[1]

$$AQY(\%) = \frac{Number\ of\ evolved\ H_2\ molecules\ \times 2}{Number\ of\ incident\ photons} \times 100\%$$

DFT Calculations

All DFT calculations were performed using the Vienna ab initio simulation package (VASP) with the Perdew-Burke-Ernzerhof (PBE) functional within the generalized gradient approximation (GGA). The projector augmented-wave (PAW) method was used to describe the interaction between core and valence electrons. A plane-wave cutoff energy of 500 eV was adopted for all calculations. Partial occupancies of the Kohn-Sham orbitals were treated using the Gaussian smearing method with a smearing width of 0.05 eV. Electronic self-consistency was achieved when the total energy change was below 1 × 10^{-5} eV, and structural optimization was considered converged when the residual forces on all atoms were less than 0.01 eV $Å^{-1}$. The heterointerface models were constructed according to the experimentally observed epitaxial relationships resolved by AC-HRTEM, namely *c*-$Cu_{2-x}S$(004)/CdS(002) and *d*-$Cu_{2-x}S$(111)/CdS(002). Commensurate supercells were built by matching the in-plane lattices of $Cu_{2-x}S$ and CdS with minimized residual mismatch. A vacuum layer of 15 Å was introduced normal to the slab direction to avoid spurious interactions between periodic images. During structural relaxation, the bottom atomic layer was fixed, while the remaining atoms were fully relaxed. For slab geometry optimization, a 3 × 3 × 1 Monkhorst-Pack k-point mesh was used, and a denser 5 × 5 × 1 mesh was applied for electronic structure calculations. Bader charge analysis was further carried out to investigate interfacial charge

redistribution among atoms.[2-5]

Table S1. Cu concentration of the seed stock dispersions and actual Cu input used in the seeded-growth experiments, as determined by ICP-OES.

Sample	Cu concentration in seed stock solution	V (ml)	Actual Cu input
c-$Cu_{2-x}S$	2.32 mg mL^{-1} (36.5 µmol mL^{-1})	1 ml	2.32 mg (36.5 µmol)
d-$Cu_{2-x}S$	23.6 mg mL^{-1} (372 µmol mL^{-1})	0.1 ml	2.36 mg (37.2 µmol)

Table S2. ICP-OES results for the Pt content after photodeposition

Sample	Corresponding Pt content (wt%)
c-$Cu_{2-x}S$	0.74
d-$Cu_{2-x}S$	0.62

Table S3. The atomic fractions of Cu, Cd, Mn, by ICP-MS.

Sample	Cd (%)	Cu (%)	Mn (%)
c-$Cu_{2-x}S$/CdS:Mn	63.05	36.83	0.12
d-$Cu_{2-x}S$/CdS:Mn	59.37	36.83	0.12

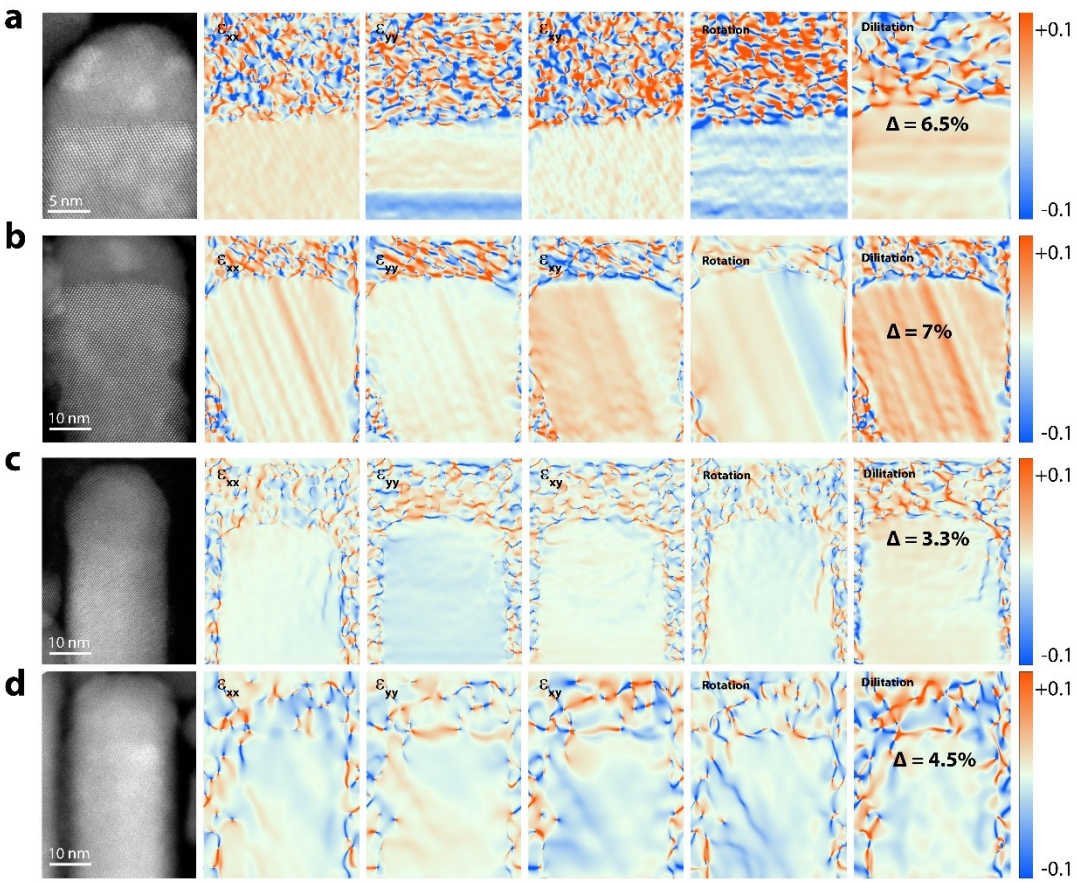

Fig. S1. Additional AC-HRTEM images and corresponding GPA dilatation maps of representative *c*-$Cu_{2-x}S$/CdS:Mn (a,b) and *d*-$Cu_{2-x}S$/CdS:Mn (c,d) heterointerfaces. The Δ maps reveal representative maximum local lattice dilatational strains of ~6.5% and ~7.0% for the covellite-derived interfaces, and ~3.3% and ~4.5% for the digenite-derived interfaces, consistent with the representative values shown in Fig. 2c,f in the main text.

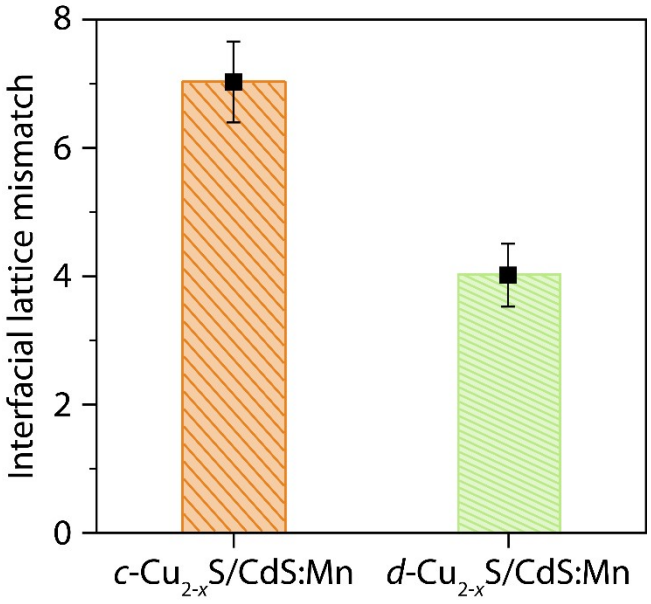

Fig. S2. Statistical comparison of the interfacial lattice mismatch between *c*-$Cu_{2-x}S$/CdS:Mn and *d*-$Cu_{2-x}S$/CdS:Mn heteronanorods, obtained from 10 independent HRTEM measurements. Error bars represent the standard deviation. The mean interfacial lattice mismatch values are 7.03 ± 0.63% for *c*-$Cu_{2-x}S$/CdS:Mn and 4.02 ± 0.49% for *d*-$Cu_{2-x}S$/CdS:Mn.

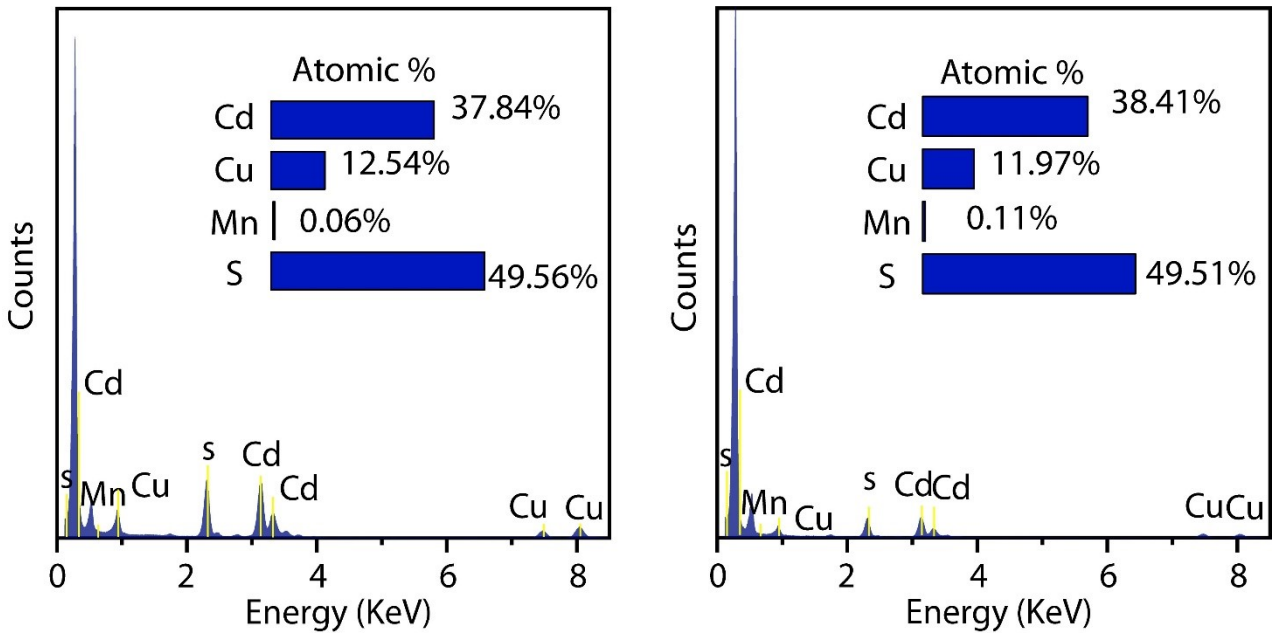

Fig. S3 EDS spectra of the heterostructures prepared from the two crystal forms in the HAADF-STEM image regions shown in Fig. 2 g,h.

Table S4. ICP-OES analysis of the post-reaction supernatants collected after the photocatalytic H_2-evolution test and subsequent centrifugation of the *c*-$Cu_{2-x}S$/CdS:Mn and *d*-$Cu_{2-x}S$/CdS:Mn heterostructures. The supernatants were heated to 60 °C and filtered to completely remove any residual solid catalyst. The concentrations of dissolved Cd and Cu ions in the filtrates were then determined by ICP-OES to evaluate possible metal-ion leaching during photocatalysis.

Sample	Element	Filterate
c-$Cu_{2-x}S$/CdS:Mn	Cu (ppm)	0.01
	Cd (ppm)	0.06
d-$Cu_{2-x}S$/CdS:Mn	Cu (ppm)	ND
	Cd (ppm)	0.02

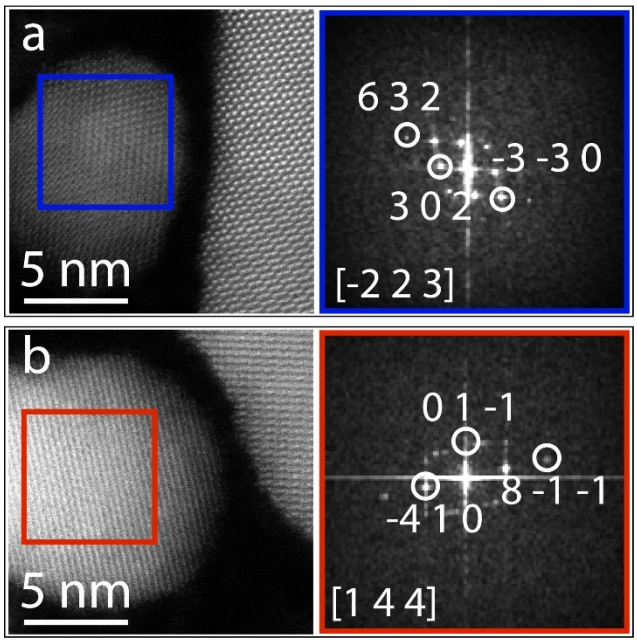

Fig. S4 AC-TEM images of representative small nanoparticles near the *c*-$Cu_{2-x}S$/CdS:Mn **(a)** and *d*-$Cu_{2-x}S$/CdS:Mn **(b)** heteronanorods and the corresponding local FFT patterns. The FFTs in (a) and (b) identify these particles as CdS, confirming that they are minor CdS nucleation byproducts formed during overgrowth rather than secondary phases or structural fragments.

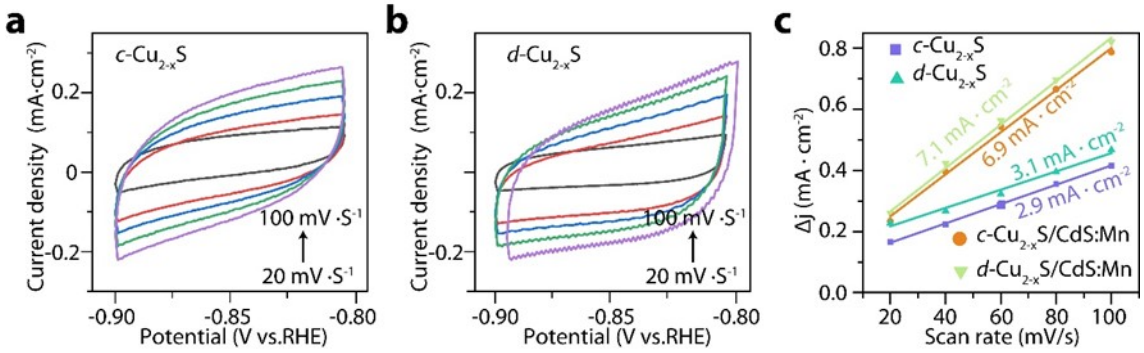

Fig. S5. (a, b) CV curves of c-$Cu_{2-x}S$ and d-$Cu_{2-x}S$ seeds at non-faradaic regions with various scan rates. **(c)** Electrochemical double-layer capacitance values calculated from CV curves measured at different scan rates in the non-Faradaic region.

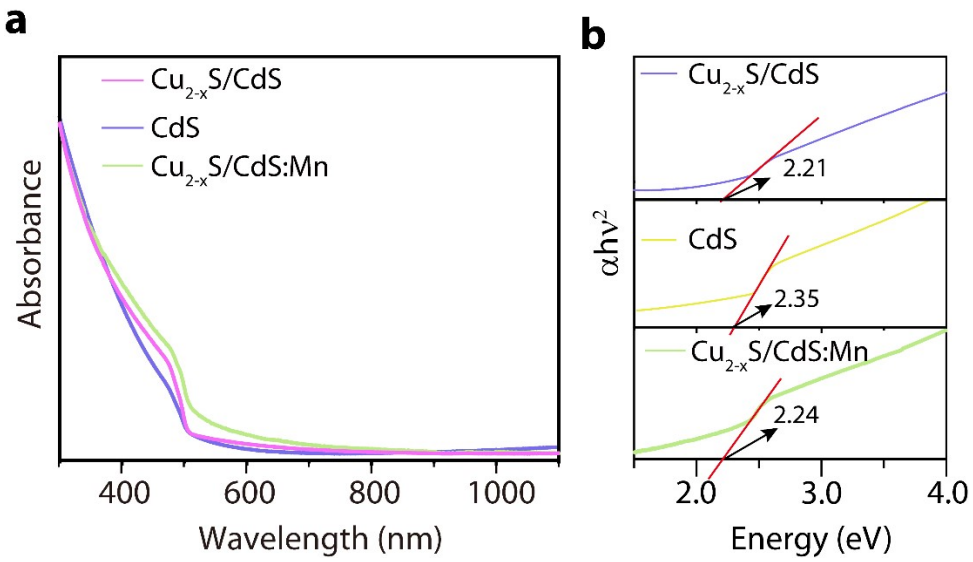

Fig. S6 UV-Vis absorption spectra (a) and corresponding Tauc plots for band gap calculation (b) of $Cu_{2-x}S$/CdS, CdS, and $Cu_{2-x}S$/CdS:Mn

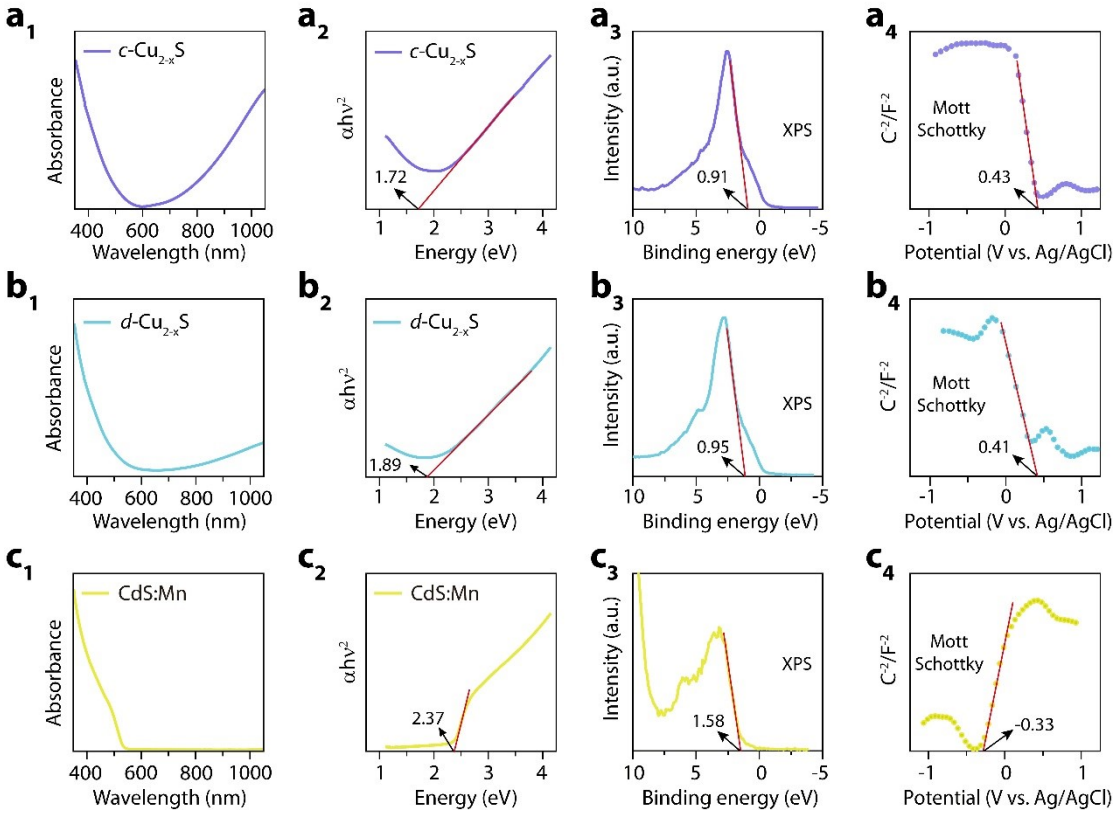

Fig. S7. (a_1, b_1, c_1) UV-Vis absorption spectra of Covellite $Cu_{2-x}S$ (a_1), Digenite $Cu_{2-x}S$ (b_1), and CdS:Mn (c_1). **(a_2, b_2, c_2)** Corresponding Tauc plots, yielding optical band gaps of 1.72 eV (Covellite), 1.89 eV (Digenite), and 2.37 eV (CdS:Mn). **(a_3, b_3, c_3)** Valence-band XPS spectra, showing valence band maxima (VBM) located at 0.91 eV (Covellite), 0.95 eV (Digenite), and 1.58 eV (CdS:Mn) below the Fermi level.**(a_4, b_4, c_4)** Mott-Schottky plots measured in the dark, estimating flat-band potentials of 0.43 V (Covellite), 0.41 V (Digenite), and -0.23 V (CdS:Mn) versus Ag/AgCl.The heterojunction exhibits a type-II band configuration, enabling spatial separation of photogenerated electrons and holes.

Method S1. Valence band potential calculated by XPS valence band spectra.

The XPS valence band spectra were presented in Fig. S7. The valence band energy (Ev) of semiconductors is derived from Equation (2).

$$E_v = \varphi + E_{VB-XPS} - 4.44 \quad (2)$$

(E_{NHE}: standard hydrogen electrodepotential; φ : electron work function of the XPS analyzer, the value was 4.2; $E_{VB\text{-}XPS}$: VB value was tested by VB-XPS)

Method S2. Valence band potential calculated by Mott-Schottky plots.

The Mott-Schottky plots were presented in Fig. S7. The flat-band potentials (E_{fb}) of semiconductor can be calculated by extrapolating the linear part of the Mott-Schottky plots to *x*-axis intercept. The Mott-Schottky plots of all samples at a frequency of 1000 Hz are presented as measured against an Ag/AgCl electrode at a pH value of 7 and recalculated against a normal hydrogen electrode (NHE) at pH 7 using Eq (3).[6]

$$V_{fb}(NHE, pH = 7) = V_{fb}(Ag/AgCl, pH_m) - [0.059 \times (7 - pH_m)] + \triangle V \quad (3)$$

where pHm is the pH value of measurement condition and △V could be ascribed as the Ag/AgCl potential against NHE which can be estimated as 0.2 eV.

The relationship between the conduction band (E_c), valence band (E_v) and flat band potentials of semiconductors can be derived from equations (4) and (5).[7]

$$E_c = E_{fb} - kTln\left(\frac{N_D}{N_c}\right) \quad (4)$$

$$E_v = E_{fb} + kTln\left(\frac{N_A}{N_V}\right) \quad (5)$$

where, N_D is the donor concentration in *n* type semiconductor and N_A is the acceptor concentration in *p* type semiconductor. N_C, N_V is the effective density of states in the conduction band and conduction band. The second term depends on the doping concentration, which for semiconductors is usually 0.1-0.2 eV.[8]

Table S5. The valence band potential (E_v) estimated by XPS valence band spectra and Mott-Schottky plots.

	c-$Cu_{2-x}S$	*d*- $Cu_{2-x}S$	CdS:Mn
E_v by XPS-VB (eV)	0.67	0.71	1.34
E_v by Mott-Schottky (eV)	0.73	0.71	1.71

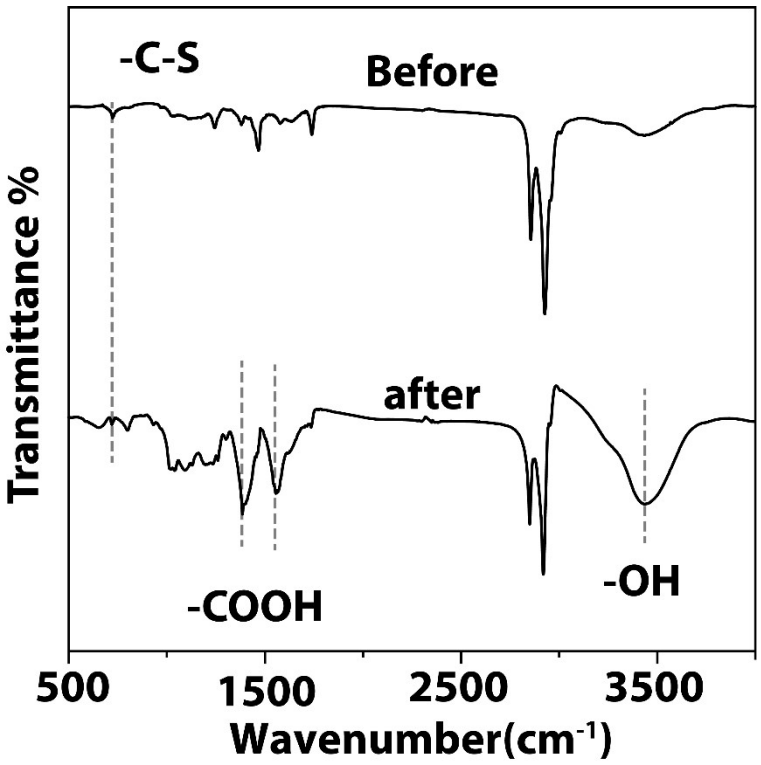

Fig. S8 FT-IR Spectra of $Cu_{2-x}S$ /CdS:Mn before and after Ligand Exchange

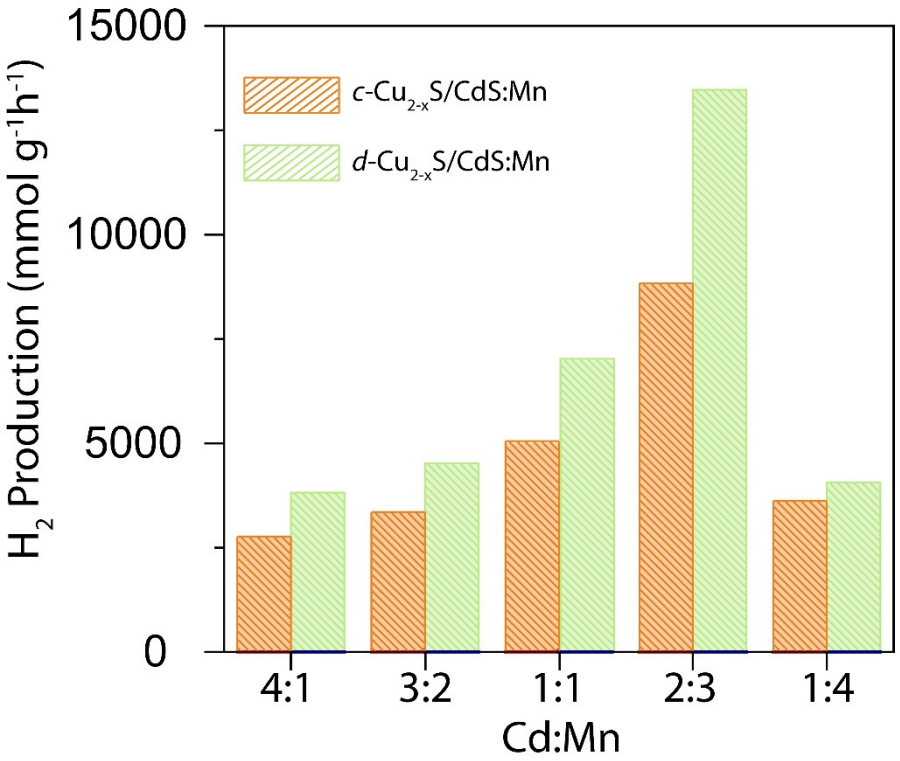

Fig. S9 Hydrogen evolution performance at different Cd:Mn feeding ratios, with the optimal performance achieved at a Cd:Mn ratio of 2:3

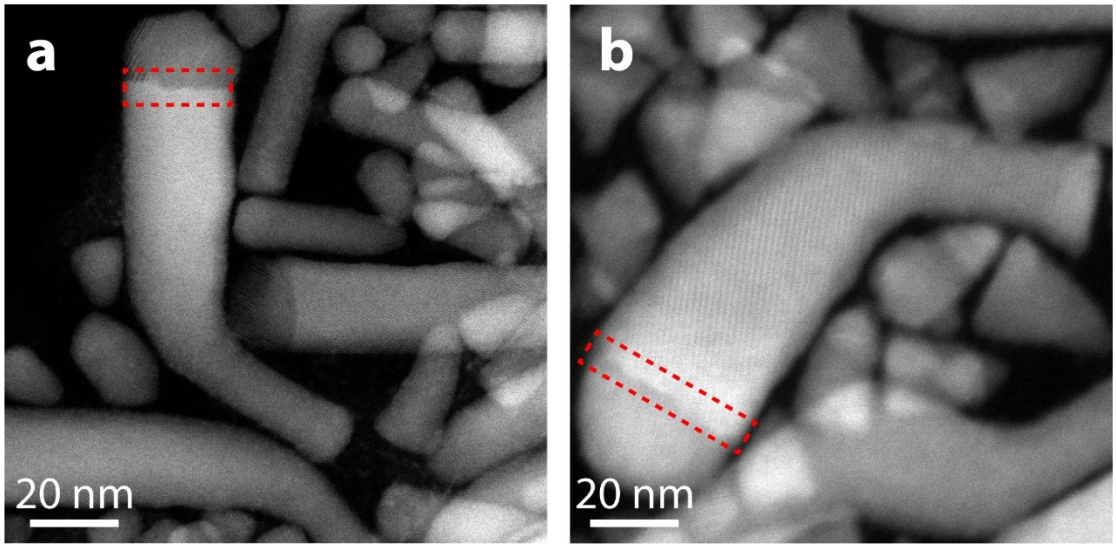

Fig. S10 TEM Images of the Heterostructures After Ligand Exchange **(a)** *c*-$Cu_{2-x}S$/CdS:Mn; **(b)** *d*-$Cu_{2-x}S$/CdS:Mn

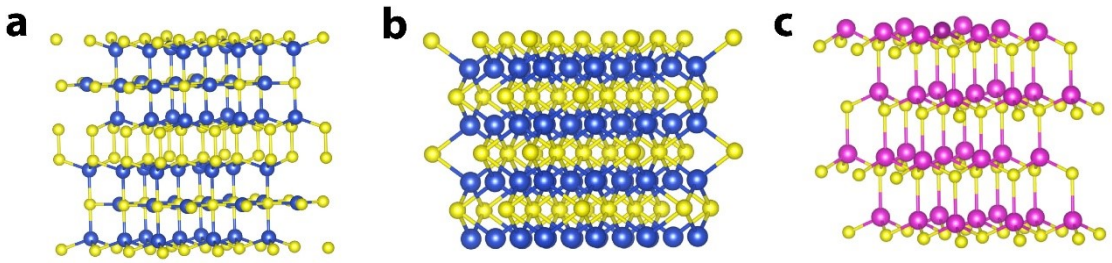

Fig. S11. Crystal structure models for DFT calculations. **(a)** *c*-$Cu_{2-x}S$; **(b)** *d*-$Cu_{2-x}S$; **(c)** CdS:Mn.

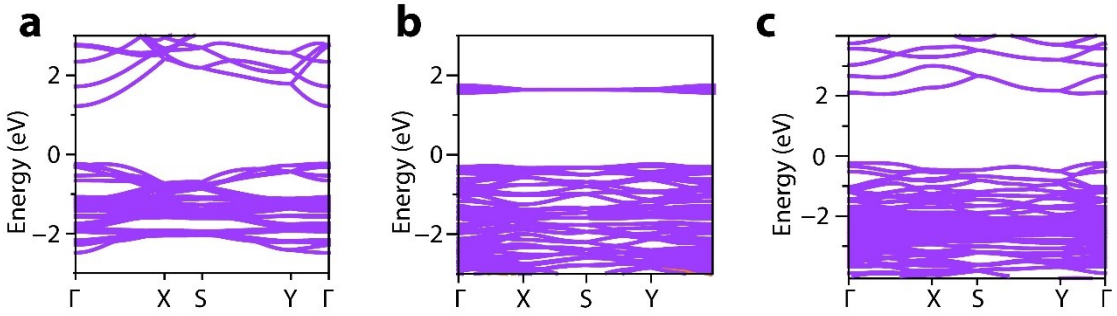

Fig. S12. Band structure for three distinct materials, with their DOS-derived bandgaps and valence band maximum (VBM) positions. **(a)** *c*-$Cu_{2-x}S$: bandgap=1.45 eV, VBM=1.20 eV; **(b)** *d*-$Cu_{2-x}S$: bandgap=1.79 eV, VBM=1.50 eV; **(c)** CdS:Mn: bandgap=2.29 eV, VBM=2.10 eV.

References

[1] Shen, Y.; Li, D.; Dang, Y.; Zhang, J.; Wang, W.; Ma, B., A ternary calabash model photocatalyst (Pd/MoP)/CdS for enhancing H_2 evolution under visible light irradiation, *Appl. Surf. Sci.,*2021, **564**, 150432.
[2] Blöchl, P. E., Projector augmented-wave method, *Phys. Rev. B,*1994, **50**, 17953-17979.
[3] Grimme, S., Semiempirical GGA-type density functional constructed with a long-range dispersion correction, *J. Comput. Chem.,*2006, **27**, 1787-1799.
[4] Kresse, G.; Furthmüller, J., Efficiency of ab-initio total energy calculations for metals and semiconductors using a plane-wave basis set, *Comput. Mater. Sci,*1996, **6**, 15-50.
[5] Perdew, J. P.; Burke, K.; Ernzerhof, M., Generalized Gradient Approximation Made Simple, *Phys. Rev. Lett.,*1996, **77**, 3865-3868.
[6] Gordanshekan, A.; Arabian, S.; Solaimany Nazar, A. R.; Farhadian, M.; Tangestaninejad, S., A comprehensive comparison of green Bi_2WO_6/g-C_3N_4 and Bi_2WO_6/TiO_2 S-scheme heterojunctions for photocatalytic adsorption/degradation of Cefixime: Artificial neural network, degradation pathway, and toxicity estimation, *Chem. Eng. J.,*2023, **451**, 139067.
[7] Di Quarto, F.; Bard, A. J., Semiconductor electrodes: Part 38. Photoelectrochemical behavior of n- and p-type GaAs electrodes in tetrahydrofuran solutions, *J. Electroanal. Chem. Interfacial Electrochem.,*1981, **127**, 43-58.
[8] Chen, X.; Huan, Y.; Sun, N.; Su, Y.; Shen, X.; Li, G.; Zhang, J.; Wei, T., Studying the variable energy band structure for energy storage materials in charge/discharge process, *Chin. Chem. Lett.,*2024, **35**, 108380.